

Fully Porous 3D Printed Titanium Femoral Stem to Reduce Stress-Shielding Following Total Hip Arthroplasty

Sajad Arabnejad,¹ Burnett Johnston,¹ Michael Tanzer,² Damiano Pasini¹

¹Department of Mechanical Engineering, McGill University, Macdonald Engineering Building, Rm 372, 817 rue Sherbrooke Ouest, Montreal, Quebec, H3A0C3, Canada, ²Division of Orthopaedics, Department of Surgery, McGill University, Jo Miller Orthopaedic Research Laboratory, Montreal, Quebec, H3G1A4, Canada

Received 4 June 2016; accepted 15 September 2016

Published online in Wiley Online Library (wileyonlinelibrary.com). DOI 10.1002/jor.23445

ABSTRACT: Current hip replacement femoral implants are made of fully solid materials which all have stiffness considerably higher than that of bone. This mechanical mismatch can cause significant bone resorption secondary to stress shielding, which can lead to serious complications such as peri-prosthetic fracture during or after revision surgery. In this work, a high strength fully porous material with tunable mechanical properties is introduced for use in hip replacement design. The implant macro geometry is based off of a short stem taper-wedge implant compatible with minimally invasive hip replacement surgery. The implant micro-architecture is fine-tuned to locally mimic bone tissue properties which results in minimum bone resorption secondary to stress shielding. We present a systematic approach for the design of a 3D printed fully porous hip implant that encompasses the whole activity spectrum of implant development, from concept generation, multiscale mechanics of porous materials, material architecture tailoring, to additive manufacturing, and performance assessment via in vitro experiments in composite femurs. We show that the fully porous implant with an optimized material micro-structure can reduce the amount of bone loss secondary to stress shielding by 75% compared to a fully solid implant. This result also agrees with those of the in vitro quasi-physiological experimental model and the corresponding finite element model for both the optimized fully porous and fully solid implant. These studies demonstrate the merit and the potential of tuning material architecture to achieve a substantial reduction of bone resorption secondary to stress shielding. © 2016 Orthopaedic Research Society. Published by Wiley Periodicals, Inc. J Orthop Res

Keywords: porous biomaterial; total hip arthroplasty; stress shielding; digital image correlation; additive manufacturing

Total hip arthroplasty (THA) is commonly used to relieve pain, restore function, and improve the quality of life for patients with compromised hip joints when conservative treatments have failed. Despite the success of THA, some of the main complications of THA, such as aseptic loosening, stress shielding, and peri-prosthetic fracture, remain a concern. Bone resorption secondary to stress shielding can be significant and arises from the mismatch of the mechanical properties between the implant and the surrounding native femoral bone.^{1,2} Materials currently used in hip implants, such as titanium-based alloys, cobalt chromium alloys, and 316L stainless steel, all have stiffness considerably higher than that of bone. Once a metal implant is implanted into the femur, most of the physiological loading is transferred to the implant, away from the comparatively more compliant surrounding bone. The altered load transfer in the implanted femur leads to the bone being under-loaded compared to its natural state. As a result bone, a living tissue that is sensitive to mechanotransduction, resorbs and loses mass by an adaptive process known as bone remodeling.³ This phenomenon is termed bone loss secondary to stress shielding.^{1,4} The reduction in bone stock can lead to serious complications, including peri-prosthetic fracture, while the mismatch

in modulus between the implant and the bone can result in thigh pain.^{5–7} Stress shielding also reduces the quality of the remaining bone stock leading to a significantly increased risk of fracture and aseptic loosening with revision surgery, should one be required. This is particularly concerning for the future, as the number of revision THAs is projected to rise, with younger patients now undergoing THA and life expectancy also increasing.

Several attempts have been made to modify femoral stems with the goal of reducing stress shielding and its adverse complications. Approaches to reduce stress shielding are mainly based on reducing the femoral stem stiffness. Methods to achieve this aim include: modification of the geometric profile of the implant, modification of its material properties, or a combination of both material and geometrical modifications. Geometric modifications include geometric variation of the stem cross section,^{8–10} stem length reduction,^{5,11,12} taper and/or curvature along the femoral stem,^{10,13} attachment of a collar or anchor at the proximal portion of the stem,^{14,15} and adoption of a hollow stem profile and internal grooves.^{1,13,16} Modifications of material properties include stem concepts with graded cellular materials from both cobalt chrome alloys as well as titanium alloys.^{17–22} Some existing works on porous materials focus on their use as surface coating on the implant to allow bone in-growth to achieve biologic fixation.^{23,24} Other works attempt to use porous materials for bone replacement, but they are mainly limited to computational modeling,^{25,26} manufacturing and testing of small samples,^{19,27,28} morphological characterization,^{29–31} and proof-of-concept implants with uniform porosity.^{19,20,32} So

Conflicts of interest: None.

Grant sponsor: Natural Sciences and Engineering Research Council of Canada (NSERC); Grant sponsor: Canadian Institutes of Health Research (CIHR).

Correspondence to: Damiano Pasini (T: 514-398-6295;

F: 514-398-7365; E-mail: damiano.pasini@mcgill.ca)

© 2016 Orthopaedic Research Society. Published by Wiley Periodicals, Inc.

far, no work has successfully tackled the challenge of using a fully porous material for femoral stems. Furthermore, there is no work that has experimentally proved the merit of tuned porous architecture to reduce stress-shielding in an implanted femur. Herein, we present a systematic approach for the design of a fully porous hip implant that encompasses the whole activity spectrum of implant development, from concept generation, multiscale mechanics of porous materials, material architecture tailoring, to 3D implant manufacturing, and performance assessment via in vitro experiments.

MATERIALS AND METHODS

Methodology of the Implant Design

Figure 1 summarizes the methodology that led to the development of the first fully porous femoral stem with tunable properties that minimize bone resorption as a result of stress shielding. A multiscale computational scheme dealing with the scale-dependent material architecture is integrated within a material tailoring scheme (Fig. 1B) to locally tune the stiffness distribution of the implant to those of the bone. Once an optimum relative density distribution solution is obtained (Fig. 1C), the result is mapped into an architected lattice ready for manufacturing (Fig. 1D). Selective Laser Melting (SLM) is used to build the implant (Fig. 1E), and micro-CT analysis of the manufactured

implant is performed to assess the fidelity of the implant micro-structure as well as to detect any entrapment of semi- or non-melted powder within the pores (Fig. 2). Finally, Digital Image Correlation (DIC) test is used to assess bone resorption performance relative to a commercially available fully solid implant of identical geometry, here used as a benchmark; a complementary Finite Element (FE) model of the experiment is also created to provide volumetric context of bone loss to the experimental results (Fig. 3). The multiscale design and material tailoring scheme for the design of a tuned fully porous hip implant is described in the section below.

Multiscale Design, Material Architecture Tailoring, and Physiological FEA of Bone Remodeling

The procedure used to develop the porous hip implant starts from the generation of a finite element model of the femoral bone which is created by processing CT-scan data of a 38-year-old patient bone. To achieve this goal, we use radiographic density of CT images, quantified as Hounsfield Unit (HU), to represent the local material properties of the human femur. The apparent density ρ for each finite element of the femur model is then determined from the Hounsfield value (HU) measured from CT data ranging from 0 to 1,567 HU. The maximum value of HU corresponds to the densest region of the cortical bone with apparent density of $2,000 \text{ kg/m}^3$. From the apparent density distribution, the effective elastic moduli of bone are

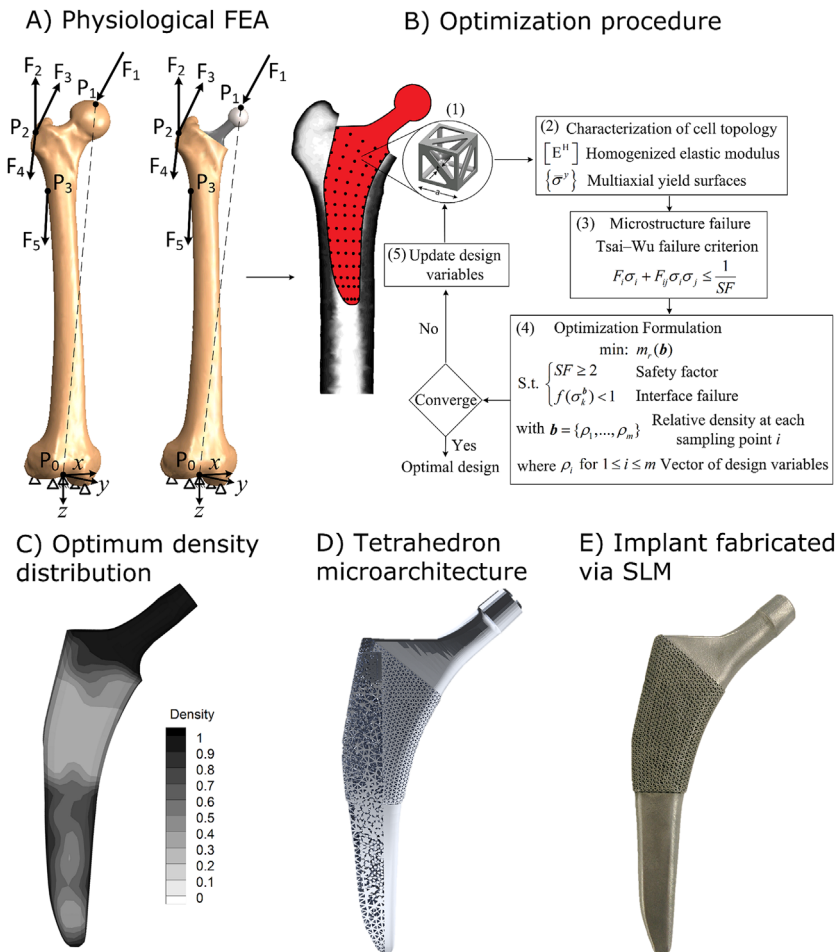


Figure 1. (A) Physiological FEA of the implanted femur. Forces F1-5, acting forces points P0-3, and boundary conditions applied to the intact and implanted femur are during the gait cycle and are taken from.^{39,40} (B) Computational scheme for multiscale mechanics and material property optimization of a minimally invasive 3D hip implant with minimum bone resorption. (C) Optimum relative density distribution of the fully porous implant. (D) Generation of lattice micro-architecture from optimal relative density distribution using a high strength tetrahedron topology. (E) Implant manufacturing via Selective Laser Melting.

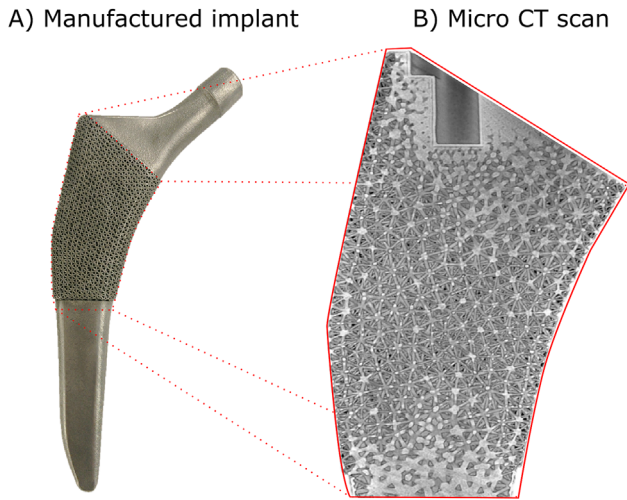


Figure 2. (A) Implant manufacturing via Selective Laser Melting. (B) Micro CT assessment of the implant lattice in the proximal region. The hole at the top left of the implant is an M6 thread which was necessary to interface with the Depuy Synthes inserter instrumentation. The inserter is identical to that of the commercial fully solid implant, and it allows to precisely control both varus-valgus as well as anteversion-retroversion positioning of the implant using the identical instrumentation that is used intraoperatively.

obtained through the relation^{33–35}:

$$\begin{cases} E = 1,904\rho^{1.64} & \rho < 0.95 \\ E = 2,065\rho^{3.09} & 0.95 < \rho \end{cases}, v = 0.3 \quad (1)$$

where E is the elastic modulus of the bone, and v is the Poisson’s ratio. Bone is treated here as isotropic material, as this simplification does not lead to a noticeable difference from those results obtained by considering orthotropic properties.^{34,35} More details on how to assign material properties to bone for finite element simulations are described in in the Supporting Information (S1).

The macro geometry of the hip implant has a tapered-wedge shape. The design domain of the prosthesis is assumed to possess a 3D lattice micro-architecture, obtained through an aperiodic tessellation of a tetrahedron based unit cell, which has been shown appropriate for both load bearing orthopaedic applications and bone ingrowth.³⁶ Mechanical properties, in particular the homogenized stiffness tensor

$[E^H]$ and the multi-axial yield surface $\{\sigma^y\}$, are calculated via Asymptotic Homogenization (AH) theory.^{26,37,38} We have shown that AH theory can capture stress distribution within the micro-structure with a considerably higher accuracy compared to other homogenization approaches.^{26,38} The effective elastic properties and yield strength as determined by AH are detailed in the Supporting Information (S2).

To obtain the optimum relative density distribution throughout the implant to minimize bone resorption secondary to stress shielding, we discretize the 3D implant domain with 75 sampling points on the medial-lateral plane of the implant, as shown in Fig. 1B and S3. The relative density at each sampling point forms the vector b of the design variables. To obtain the relative density distribution throughout the implant, we considered four sampling points as a 4-node bilinear quadrilateral element. The relative density of each element of the implant FE model is then obtained from the linear interpolation between the relative densities of the nodes of the 4-node bilinear element. Details on how to assign relative density distribution throughout the implant are given in Supporting Information S3.

The interior micro-architecture of the implant (Fig. 1D) is obtained for a femur loaded under the physiological loading and boundary conditions,^{39,40} as shown in Table 1 reporting force location and their values.

Material architecture tailoring is achieved by minimizing bone resorption, $m_r(b)$, subjected to a set of inequality constraints, including the fatigue safety factor, $SF \geq 2$, and the interface failure, $f(\sigma_k^b) < 1$. We use the Tsai–Wu failure criterion for the failure analysis of the tetrahedron lattice under multi-axial and fatigue conditions. To design against fatigue failure, we assume the lattice micro-structure to be free of defects, such as scratches, notches, and nicks. As a result, the constant life diagram can be constructed to verify and design the lattice against fatigue failure.⁴¹ Detailed formulations for multiscale and fatigue design of porous microstructure are provided in the Supporting Information S4. The amount of bone loss around the stem is determined by assessing the amount of bone that is under loaded post implantation relative to the intact femur. Bone can be considered locally under loaded when its local strain energy (U) per unit of bone mass (ρ) ($S = \frac{U}{\rho}$), is beneath the local reference value S_{ref} , which is the value of S when no prosthesis is present. Bone resorption starts when the local value of S is beneath the value of $(1 - s) S_{ref}$.^{42,43} s is the threshold level or dead zone. In this study, the value of dead zone is set to be 0.75.⁴³ The interface failure $f(\sigma_k^b)$ is

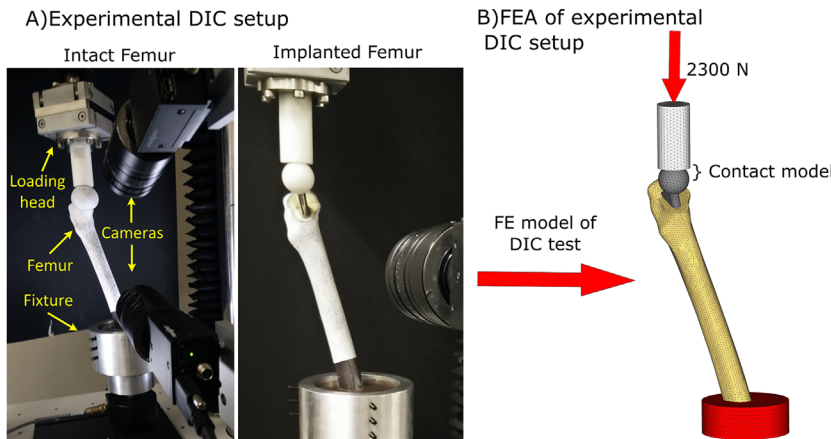


Figure 3. (A) In vitro assessment of stress shielding using Digital Image Correlation (DIC) and (B) FE model of DIC test.

Table 1. Forces, Acting Forces Points, and Boundary Conditions Applied to the Intact and Implanted Femur During the Gait Cycle (Taken From^{33,34})

Force (N)				Location (m)			
Load cases	X	Y	Z	Points	X	Y	Z
F_1	-486	-295.2	2062.8	P_0	0	0	0
F_2	64.8	104.4	-118.8	P_1	0.035	0.009	-0.449
F_3	522	38.7	-778.5	P_2	-0.039	-0.018	-0.41
F_4	-4.5	-6.3	171	P_3	-0.022	-0.01	-0.375
F_5	-8.1	-166.5	836.1				

expressed by $f(\sigma_k^b) = \frac{\tau}{S_s} < 1$, where τ is the local shear stress at the bone-implant interface, and S_s is the bone shear strength. The interface failure $f(\sigma_k^b)$ is constrained to be lower than one to ensure the bone-implant interface failure will not occur. Detailed formulation for bone loss measurement and interface failure are presented in the Supporting Information S5. Through this process of material property tailoring, an implant with tuned high strength porous architecture that realizes minimum bone resorption is obtained. The implant is then manufactured with SLM technique, as described in the following section.

Manufacturing

The internal micro-architecture of the implant is generated from the relative density distribution determined from the optimization process previously described. The relative density of each tetrahedron lattice is obtained by calculating the average relative density over the lattice using a Gauss quadrature integration technique with one Gauss point. SLM constraints and bone in-growth requirements, including minimum manufacturable strut thickness, porosity, and pore size, are also considered during the development of the micro-architecture. In particular, the proximal portion of the hip replacement stem is constrained for optimum pore size and porosity to allow for early and extensive bone in-growth.³⁶ Pore size of 500 μm and porosity of 70% are designed on the surface of the proximal bone apposing section of the hip implant. The minimum strut thickness is constrained to 200 microns throughout the implant to ensure manufacturability. The architected fully porous implant is manufactured with Selective Laser Melting (SLM) by Renishaw AM250 (Renishaw Limited, Mississauga, ON) with a power of 200 W and energy density of 60 J/mm³ (Fig. 1E). The laser spot diameter is 70 μm . The powder size is between 15 and 50 μm , and the powder layer of 30 μm is used. The part is processed at 720° Celsius under argon for 2 h, and is removed from the build plate post treatment using EDM wire cutting.

To assess the quality of the manufactured internal architecture, the implant is scanned using a Nikon Xt H225 ST (Nikon Canada, Mississauga, ON) (high-resolution micro-CT) (Fig. 2B). Detailed inspection of CT-scan images confirms mechanical integrity of each cell strut with complete formation of all the struts with neither break nor discontinuity among the elements and absence of loose powder particles within the cell pores. To assess bone resorption performance for the manufactured implant, a benchtop biomechanical test and a complementary FE model of the experiment are conducted to provide volumetric context of stress and strain variation in composite femora subjected to quasi-physiologic loading conditions.

Experimental Evaluation: DIC Evaluation With Complementary FEA

To demonstrate the methodological approach followed in this work, a set of complementary in vitro DIC test and computational investigations are conducted on a simplified model. The simplified model utilizes artificial composite femurs (Sawbones[®], Vashon, WA) under quasi-physiological loading conditions in order to minimize the variability between samples. This allows a clearly controlled experimental set up that demonstrates the experimentally measured performance of a graded fully porous implant compared to an identical clinically available fully solid titanium alloy implant of equal geometry (Trilock BPS, DePuy, Warsaw, IN), our benchmark. A total of six femurs are used, with three femurs randomly allocated to each treatment to receive either the fully porous or the solid control stem. The fourth generation femurs from Sawbones[®] are selected for their claimed ability to reproduce a biomechanical behavior similar to that of fresh cadaver specimens as well as low inter-specimen variability.⁴⁴ Sawbones[®] femurs are made of a solid material representing the cortical bone, and a foam representing the trabecular bone. Although Sawbones[®] femurs provide a basic tissue differentiation between the cortical and trabecular bone, we emphasize their material properties are still isotropic ($E = 16.7 \text{ GPa}$ for the solid material, and $E = 0.155 \text{ GPa}$ for the foam); the foam, in particular, has uniform relative density, that cannot represent the actual femoral anisotropy of native trabecular bone.

The first study considers a quasi-physiological loading pattern that can be precisely reproduced in vitro. The goal is to compare changes in surface strain relative to an intact composite femur as a bench top experimental estimate of the expected in vivo stress shielding. The experiment set up consists of a digital image calibration (DIC) system calibrated to measure the surface strain of both intact and implanted femurs during loading. The change of strain, measured on the medial aspect of the femur, is used as an experimental proxy for stress shielding. For the experimental preparation, all femoral condyles are resected at a distance of 22 cm measured from the tip of the greater trochanter. Using a customized fixture, the femurs are angled at 12° flexion, and 12° adduction, and potted into epoxy (detailed description provided in the Supporting Information S6). The femoral head is loaded up to 2300 N through a fixture that is free to translate within the transverse plane such that there is no un-physiological moment applied. A stereo mounted camera set up is used to acquire synchronized images of the medial calcar and medial aspect of the femur covering Gruen zones 4 through 7.⁴⁵ The surface of the composite femora are speckle painted to achieve a distribution of speckles ranging

from 500 to 1,000 microns (Fig. 3A), as described in detail in the Supporting Information S7. Images are taken at a frequency of 6Hz starting from an unloaded state, up to the maximum load at 2300N using five MP CCD cameras (Point Grey Research Inc., Richmond, BC) with Fujinon 25 mm c-mount lenses (Fujifilm, Valhalla, NY). From the recorded image, digital calibration is performed using Vic-3D (Correlated Solutions, Irmo, SC). The stereoscopic camera system is attached directly to an electromechanical testing frame (Bose 3510 electroforce—Bose, Eden Prairie, MN) using a custom fixture to ensure consistent camera position. The femurs are then randomly allocated to receive either the fully porous or the control stem (Supporting Information S8). An Anterior-Posterior (AP) and Medial-Lateral (ML) radiograph are taken to ensure consistent implant position, as well as correct neck offset and length (Fig. S6, Supporting Information S9). The DIC data for each individual femur is exported and registered to an atlas femur using an iterative process involving closest point minimization (Figs. S7–8, Supporting Information S10). This ensures that each local strain measurement is reliably and anatomically located across all femurs.

To be consistent with strain energy measurements used in bone loss measurement during the design process, we considered as a metric for bone resorption, the ratio of post implantation surface strain to the pre-implantation surface strain squared. Using the principle compressive strain, we can roughly estimate the strain energy of each element as follows:

$$S_{\text{elm}} = \frac{1}{2} \varepsilon_{\text{pc}}^2 E V_{\text{elm}} \quad (2)$$

where S_{elm} is the strain energy of an element, ε_{pc} is the principle compressive strain, E is the Young's modulus of the element material, and V_{elm} is the element volume. If we consider S_{ref} as the local strain energy before implantation, the ratio of the strain energy of element material on the surface of the composite femur after and before implantation is as follows:

$$\frac{S_{\text{elm}}}{S_{\text{ref}}} = \left(\frac{\varepsilon_{\text{pc}}}{\varepsilon_{\text{pc}(\text{ref})}} \right)^2 \quad (3)$$

Equation 3 shows that the strain energy before and after implantation can be related to the ratio of the post implantation surface strain and the pre-implantation surface strain squared. Therefore, in this work Equation 3 was adopted as metric for bone loss measurement on the surface of the composite femur. If the reduction of strain after implantation is greater than 50% relative to the intact femur, the bone surface region is deemed to be prone to bone resorption (Supporting Information S11). This value is chosen to coincide with the physiological FEA model value for the dead zone threshold (Supporting Information S5) used to design the architected stem (Fig. 1B). The percentage of surface susceptible to bone resorption is compared between the fully porous and solid control stem for Gruen Zones 5 through 7 using a two tailed student t -test with $p < 0.05$, which is considered statistically significant.

One limitation of the experimental technique described above is that only surface strain can be recorded. Bone resorption secondary to stress shielding, however, is a volumetric phenomenon. To address this issue, we conduct FE simulations replicating the experimental conditions of

the implanted femur (Fig. 3B) with the goal of obtaining volumetric measures of bone resorption that would supplement the surface strain measure obtained experimentally. For this purpose, a 3D model of the composite femur is created from an accurate reconstruction of CT-scan data, and FE simulations with loading and boundary conditions equivalent to those used in the experiments, are conducted in pre- and post-implantation conditions. The isotropic properties of the Sawbones[®] femur (Young's modulus: 16.7 GPa for cortical bone and 0.155 GPa for trabecular bone) are used for the computational model. The strain energy of the bone before and after implantation is measured to calculate bone loss via the criterion used during the material tailoring process. The percentage of bone loss on the bone surface is also measured and compared with the DIC results to bolster the experimental measures of bone loss in the fully porous titanium alloy stem and the fully solid titanium alloy control stem. The results are segregated into radiological Gruen zones that are commonly used to clinically assess the performance of THA.^{46,47}

RESULTS

Material Tailoring and Physiological FEA

The material architecture tailoring described in the methodology section resulted in the optimum density distribution shown in Fig. 1C. The amount of bone resorption for the optimized implant is presented in Fig. 4 and compared with the amount of bone resorption of a fully solid implant. The physiological FEA model (Fig. 4) shows a total of 34% of bone resorption secondary to stress shielding for the fully solid implant, and 8% in the optimized fully porous implant. This indicates a greater than 75% reduction in bone loss secondary to stress shielding. The fully porous implant can realize 8% volumetric bone loss in Gruen zone 7, whereas the fully solid implant 27% in zone 7, followed by 5% and 2% bone loss in Gruen zones 6 and 2, respectively. This shows that the amount of bone resorption for the fully porous implant is mainly limited to the proximal region in Gruen zone 7, whereas for the fully solid implant the amount of bone resorption extends to the distal region zone 6.

Manufacturing

Figure 1D shows the mapping of the optimum material distribution into a tessellated tetrahedron micro-architecture. The reduced bone apposing pore size can clearly be seen, targeting an average of 500 microns for optimum bone in-growth. CT scanning inspection shows no gross malformations of struts or entrapped un-melted powder. Figure 2B shows the CT visualization of the internal micro-architecture of the manufactured implant.

Experimental Evaluation: DIC With Complementary FEA

Figure 5 shows the results of the quasi-physiological DIC experimental model and the corresponding FEA model for both the optimized fully porous and fully solid implant. The DIC experiment shows the greatest change in strain in the proximal medial calcar in Gruen zone 7, with bone loss of $70 \pm 24\%$ for the fully

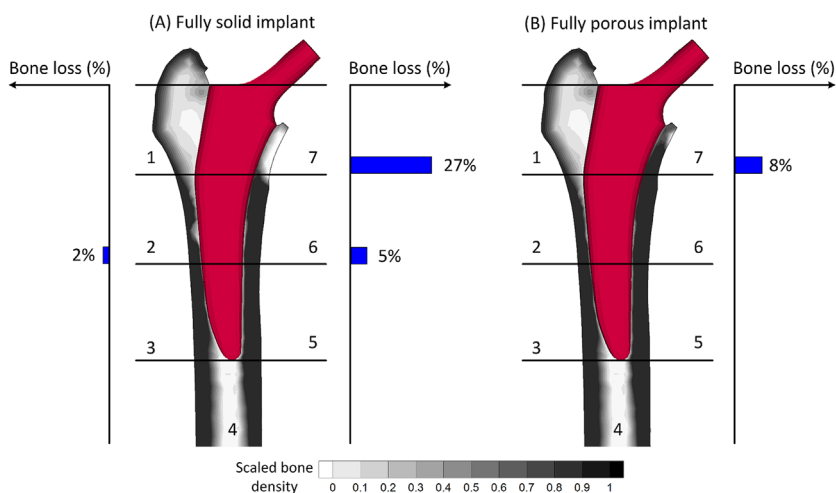


Figure 4. Regions prone to bone resorption in Gruen zones 1–7 for (A) fully solid implant and for (B) fully porous implant with tailored relative density distribution. Values presented here are volume bone loss measured from the metric described in the Supporting Information S5. All zones with no reported bone resorption are 0%.

solid implant and $71 \pm 14\%$ for the fully porous implant ($p > 0.05$). Gruen zone 6 shows a statistically significant reduction in strain shielding for the fully porous implant as compared to the fully dense implant ($25 \pm 5\%$ vs. $7 \pm 7\%$ $p < 0.05$). Gruen zone 5 reports the least amount of strain shielding for both implants, $7 \pm 10\%$ and $2 \pm 3\%$, respectively for the fully solid and fully porous implants ($p > 0.05$). The medial diaphysis distal to the implant shows no variation in strain from the intact femur for both the optimum and fully solid prostheses. This indicates that the neck offset is appropriately established after implantation, thereby eliminating any systematic experimental bias of the stress shielding results. The corresponding FEA model provides both surface strain reduction as well as the volumetric change of strain for both implants. Gruen zone 7 shows the largest amount of stress shielding with a 27% and 16% volumetric reduction of bone for the fully solid and optimum porous implant, respectively. This shows 40% reduction of volume bone loss for the fully porous implant. In Gruen zone 6, the amount of volume bone loss for the fully solid implant is 14%; for the fully porous implant this value is equal to 2%, 78% lower than that for the baseline implant. Gruen zone 5 shows no variation between the implanted and intact femur for both implants.

At Gruen zone 7, the amount of surface bone loss for fully solid and fully porous implant is 86% and 71%, respectively. The extent of bone resorption at Gruen zone 6 for the fully dense implant is significantly higher compared to the fully porous implant. The amount of surface bone resorption for the fully porous implant is 8%, whereas for the fully solid implant this value is 36%. This shows 77% reduction of surface bone loss for the fully porous implant at Gruen zone 6 compared to fully solid implant. At Gruen zone 5, no surface bone resorption is observed for both fully porous and fully solid implant.

DISCUSSION

The results from both the physiological finite element model and the DIC experiment of the current study

show a reduction in stress shielding of the porous implant as compared to a fully solid stem of identical geometry. Furthermore, CT analysis shows that the optimum relative density distribution could be mapped into an aperiodic lattice domain with no entrapped unmelted powder. This indicates that the hip implant is the first to be fully porous throughout, in contrast to existing stems with a porous coating on a solid part.

Previous designs relying on the modification of the material properties of femoral stems aimed at preserving bone stock have been used, with varying degrees of success. Isoelastic composite stems, introduced in the 1970s by Robert Mathys, were designed with a stainless steel core to improve the mechanical strength, and a polyacetal resin layer with elastic modulus similar to that of bone to avoid stress-shielding.⁴⁸ The results of 15 years follow-up revealed this prosthesis to perform extremely poorly.⁴⁹ Another composite implant is the EPOCH hip stem, which has a forged cobalt-chromium-molybdenum core section with an outer layer of pure titanium fiber metal mesh applied over a polyaryletherketone (PAEK) middle section.⁵⁰ While the data of 5 years follow-up suggest that this fully porous-coated implant design provides fixation and better maintained peri-prosthetic cortical thickness and density than conventional implants,⁵¹ a recent study has demonstrated a 10–20% loss in peri-prosthetic bone at 7 years. This is very similar to that seen with a conventional stem.^{51,52} The authors concluded that the merit of the Epoch stem in preserving bone mineral is only transient in nature. This can be likely attributed to the homogeneous and uniform material distribution of the stem no longer being truly isolelastic. In contrast, the implant presented in this work has shown that optimal properties gradients enable the realization of a fully porous implant with properties that mirror the normally changing density of the surrounding proximal femoral bone.

On the other hand, other fully porous materials that commercially available today are less stiff than the solid substrate materials, but do not provide a

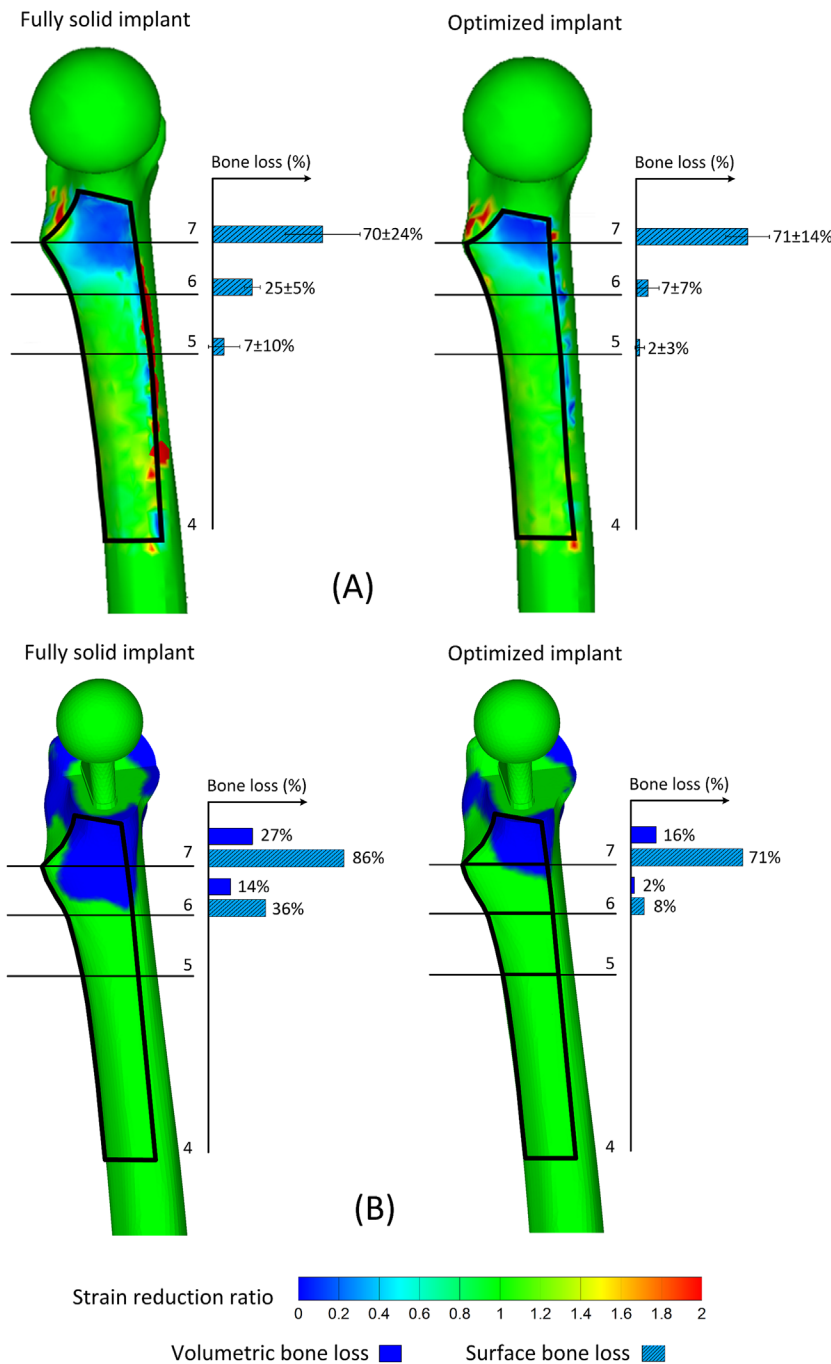


Figure 5. (A) Surface bone loss measurement obtained from DIC experiment. (B) Surface and volume bone loss measurement from the FE model reproducing the condition of the experiment set-up. Surface bone loss is considered when the ratio of post implantation surface strain squared to the pre implantation surface strain squared decreases more than 75%. Volume bone loss is measured when the ratio of post implantation strain energy to the pre implantation strain energy decreases more than 75%.

viable option for creating an isoelastic femoral stem. An example is porous tantalum which is excellent for its biocompatibility, high volumetric porosity, and low modulus of elasticity, but its pore distribution is predominantly uniform. The reduced stiffness of tantalum foam, in fact, decreases bone resorption; yet, its homogenous distribution of pores has the undesirable effect of increasing interface stresses.^{43,53,54} In addition, its use in femoral stems can only be as a porous coating on a stiffer solid titanium substrate, precluding a fully porous stem. As a result, most, if not virtually all of the advantages of its low modulus of elasticity, are lost when it is applied for use in a

femoral hip stem. The stem design in this study not only addresses the issue of stress shielding by its graded and fully porous design, but also allows the stem to have sufficient strength; its porous architecture is obtained from an aperiodic tessellation of a tetrahedron based unit cell, which has been shown appropriate for load bearing orthopaedic applications.³⁶

The volumetric index of bone loss has significant clinical relevance since this corresponds to the bone stock available for revision surgeries. We found a reasonably good agreement between the amounts of surface bone loss from FEA and those from DIC

experiments. The figures show that FEA results are within statistic values obtained from DIC experiments. We can thus, assume the volumetric bone loss measured from simulations can reasonably assess the actual amount of stress shielding that might occur during the DIC experiment. This indicates the reduction of the surface strain is an appropriate proxy for stress shielding.

Although the reduced complexity of the experimental set up shows a promising reduction in stress shielding, cadaveric match pair femurs with physiological loading conditions should be used to reproduce the conditions for which the implant is designed. This is a part of future study. In addition, since the bone loss measured in this study do not account for the adaptive process of bone remodeling over time,^{55,56} their values are still representative of the amount of bone resorption from 6 to 24 months post-operatively.⁵⁷ Although the majority of bone remodeling occurs within 2 years, Bone Mass Density can continue to decrease as a result of stress shielding even up to 14 years after implantation.⁵⁷ In this case, the amount of bone resorption can be detected with dual-energy X-ray absorptiometry (DEXA) with a precision of 1–4%.⁵⁷

The implications of the work here undertaken are very promising, serving as a multidisciplinary bridge integrating biomechanics, material property tuning, additive manufacturing of 3D porous architecture, and clinically relevant experiments, all addressing shortcomings of existing materials for hip prostheses. We have demonstrated that three-dimensional material distributions with variable stiffness can be obtained to develop a hip stem, which is shaped into a minimally invasive geometry. The stem is a short and has a single tapered wedge design, which is the most common implant design type used in North America.⁵⁸ In this study, we also showed the effectiveness of using SLM technology to build Ti-6AL-4V controlled gradients of fully porous micro-architected stems.

Unsurprisingly, care must be taken also here with interpreting the results of this work and extrapolate a direct assessment of expected clinical outcomes. Bone resorption is a complex phenomenon involving a multitude of factors specific to the implant, the patient, the surgical procedure, and varying degrees of interaction between the aforementioned factors. It is important to underline that the values reported for stress shielding are percentages of bone that are susceptible to stress shielding immediately post operation, and not necessarily the bone tissue that will resorb in the long term. Although numerical techniques are available to represent this process that is time dependent, at the present time there are no widely-accepted in vitro biomechanical models available that can represent the phenomenon. As such, further experimental validation of the ability of a tuned fully porous implant to reduce stress shielding should rely upon long term in vivo models that can account for the biomechanical interaction complexity of a living system. Future work includes

replicating the current investigation in an animal model to examine the long-term bone remodeling of a fully porous implant.

CONCLUSION

A high strength fully porous material with tunable mechanical properties is introduced for use in minimally invasive hip replacement. The implant micro-architecture is fine-tuned to locally mimic bone tissue properties, which results in minimum bone resorption secondary to stress shielding. This work demonstrates that a high strength fully porous femoral stem with tunable mechanical properties can be designed and manufactured to reduce stress-shielding. The proposed implant has been built successfully with SLM technique while respecting bone in-growth requirements at the implant interface. The in vitro test has proved substantial decrease of the femur surface strain, inferring substantial reduction in stress shielding. This development is promising and may possibly pave the way for tuned fully porous materials for bone interfacing implants of next generation use in orthopaedic arthroplasty surgery.

AUTHORS' CONTRIBUTIONS

SA had substantial contributions to research design, finite element simulation, optimization of the hip implant, interpretation of data, and drafting the paper. BJ had substantial contributions to research design, design of experiment, the acquisition and interpretation of experimental data, and drafting the paper. MT had substantial contributions to research design, clinical evaluation, drafting the paper, and revising it critically. DP had substantial contributions to problem formulation and research design, computational mechanics and implant optimization, supervision, drafting, and revising the paper besides approval of the submitted and final versions. All authors have read and approved the final submitted manuscript.

REFERENCES

1. Glassman A, Boby J, Tanzer M. 2006. New femoral designs do they influence stress shielding? *Clin Orthop Relat Res* 453:64–74.
2. Boby J, Mortimer E, Glassman A, et al. 1992. Producing and avoiding stress shielding: laboratory and clinical observations of noncemented total hip arthroplasty. *Clin Orthop Relat Res* 274:79–96.
3. Chamay A, Tschantz P. 1972. Mechanical influences in bone remodeling. Experimental research on Wolff's law. *J Biomech* 5:173–180.
4. Sumner DR, Turner TM, Igloria R, et al. 1998. Functional adaptation and ingrowth of bone vary as a function of hip implant stiffness. *J Biomech* 31:909–917.
5. Bugbee WD, CULPEPPER WJ, Engh CA, et al. 1997. Long-term clinical consequences of stress-shielding after total hip arthroplasty without cement. *J Bone Joint Surg* 79:1007–1012.
6. Engh CA Jr, Young, Engh CA Sr, et al. 2003. Clinical consequences of stress shielding after porous-coated total hip arthroplasty. *Clin Orthop Relat Res* 417:157–163.

7. McAuley JP, Culpepper WJ, Engh CA. 1998. Total hip arthroplasty: concerns with extensively porous coated femoral components. *Clin Orthop Relat Res* 355:182–188.
8. Fernandes PR, Ruben RB, Folgado J. 2010. Bone implant design using optimization methods. In: Ochsner A, Ahmed W, editors. *Biomechanics of hard tissues: Modeling, testing, and materials*. New York: John Wiley. p 267–296.
9. Ruben R, Folgado J, Fernandes P. 2007. Three-dimensional shape optimization of hip prostheses using a multicriteria formulation. *Struct Multidisc Optim* 34:261–275.
10. Kim Y-H, Kim J-S, Cho S-H. 2001. Strain distribution in the proximal human femur. *Bone Joint J* 83:295–301.
11. Niinimäki T, Junila J, Jalovaara P. 2001. A proximal fixed anatomic femoral stem reduces stress shielding. *Int Orthop* 25:85–88.
12. Renkawitz T, Santori FS, Grifka J, et al. 2008. A new short uncemented, proximally fixed anatomic femoral implant with a prominent lateral flare: design rationals and study design of an international clinical trial. *BMC Musculoskelet Disord* 9:147.
13. Schmidt J, Hackenbroch M. 1994. The Cenos hollow stem in total hip arthroplasty: first experiences in a prospective study. *Arch Orthop Trauma Surg* 113:117–120.
14. Crowninshield R, Brand R, Johnston R, et al. 1980. An analysis of femoral component stem design in total hip arthroplasty. *J Bone Joint Surg* 62:68–78.
15. Behrens B, Wirth C, Windhagen H, et al. 2008. Numerical investigations of stress shielding in total hip prostheses. *Proc Inst Mech Eng H* 222:593–600.
16. Mattheck C, Vorberg U, Kranz C. 1990. Effects of hollow shaft endoprosthesis on stress distribution in cortical bone. *Biomed Tech* 35:316–319.
17. Hazlehurst KB, Wang CJ, Stanford M. 2013. The potential application of a cobalt chrome molybdenum femoral stem with functionally graded orthotropic structures manufactured using laser melting technologies. *Med Hypotheses* 81:1096–1099.
18. Hazlehurst KB, Wang CJ, Stanford M. 2014. A numerical investigation into the influence of the properties of cobalt chrome cellular structures on the load transfer to the periprosthetic femur following total hip arthroplasty. *Med Eng Phys* 36:458–466.
19. Murr L, Gaytan S, Medina F, et al. 2010. Next-generation biomedical implants using additive manufacturing of complex, cellular and functional mesh arrays. *Philos Transac A Math Phys Eng Sci* 368:1999–2032.
20. Marcellin-Little DJ, Cansizoglu O, Harrysson OL, et al. 2010. In vitro evaluation of a low-modulus mesh canine prosthetic hip stem. *Am J Vet Res* 71:1089–1095.
21. Arabnejad S, Pasini D. 2012. Multiscale design and multi-objective optimization of orthopedic hip implants with functionally graded cellular material. *J Biomech Eng* 134:031004.
22. Arabnejad S, Pasini D. 2013. The fatigue design of a bone preserving hip implant with functionally graded cellular material. *J Med Dev* 7:020907.
23. Harrison N, McHugh P, Curtin W, et al. 2013. Micromotion and friction evaluation of a novel surface architecture for improved primary fixation of cementless orthopaedic implants. *J Mech Behav Biomed Mater* 21:37–46.
24. Marin E, Fusi S, Pressacco M, et al. 2010. Characterization of cellular solids in Ti6Al4V for orthopaedic implant applications: trabecular titanium. *J Mech Behav Biomed Mater* 3:373–381.
25. Khanoki SA, Pasini D. 2012. Multiscale design and multi-objective optimization of orthopedic hip implants with functionally graded cellular material. *J Biomech Eng* 134:031004.
26. Arabnejad Khanoki S, Pasini D. 2013. Fatigue design of a mechanically biocompatible lattice for a proof-of-concept femoral stem. *J Mech Behav Biomed Mater* 22:65–83.
27. Cheng XY, Li SJ, Murr LE, et al. 2012. Compression deformation behavior of Ti-6Al-4V alloy with cellular structures fabricated by electron beam melting. *J Mech Behav Biomed Mater* 16:153–162.
28. Parthasarathy J, Starly B, Raman S, et al. 2010. Mechanical evaluation of porous titanium (Ti6Al4V) structures with electron beam melting (EBM). *J Mech Behav Biomed Mater* 3:249–259.
29. Xia Z, Zhou C, Yong Q, et al. 2006. On selection of repeated unit cell model and application of unified periodic boundary conditions in micro-mechanical analysis of composites. *Int J Solids Struct* 43:266–278.
30. Mullen L, Stamp R, Fox P, et al. 2009. Selective laser melting: a unit cell approach for the manufacture of porous, titanium, bone in-growth constructs, suitable for orthopedic applications II. Randomized structures. *J Biomed Mater Res B Appl Biomater* 92:178–188.
31. Ahmadi S, Campoli G, Amin Yavari S, et al. 2014. Mechanical behavior of regular open-cell porous biomaterials made of diamond lattice unit cells. *J Mech Behav Biomed Mater* 34:106–115.
32. Eldesouky I, Abdelaal O, El-Hofy H. 2014. Femoral hip stem with additively manufactured cellular structures. *Biomedical Engineering and Sciences (IECBES), 2014 IEEE Conference on: IEEE*. p 181–186.
33. Austman RL, Milner JS, Holdsworth DW, et al. 2008. The effect of the density-modulus relationship selected to apply material properties in a finite element model of long bone. *J Biomech* 41:3171–3176.
34. Baca V, Horak Z, Mikulenka P, et al. 2008. Comparison of an inhomogeneous orthotropic and isotropic material models used for FE analyses. *Med Eng Phys* 30:924–930.
35. Peng L, Bai J, Zeng X, et al. 2006. Comparison of isotropic and orthotropic material property assignments on femoral finite element models under two loading conditions. *Med Eng Phys* 28:227–233.
36. Arabnejad S, Johnston RB, Pura JA, et al. 2016. High-strength porous biomaterials for bone replacement: a strategy to assess the interplay between cell morphology, mechanical properties, bone ingrowth and manufacturing constraints. *Acta Biomater* 30:345–356.
37. Masoumi Khalil Abad E, Arabnejad Khanoki S, Pasini D. 2013. Fatigue design of lattice materials via computational mechanics: application to lattices with smooth transitions in cell geometry. *Int J Fatigue* 47:126–136.
38. Arabnejad S, Pasini D. 2013. Mechanical properties of lattice materials via asymptotic homogenization and comparison with alternative homogenization methods. *Int J Mech Sci* 77:249–262.
39. Heller MO, Bergmann G, Kassi JP, et al. 2005. Determination of muscle loading at the hip joint for use in pre-clinical testing. *J Biomech* 38:1155–1163.
40. Speirs AD, Heller MO, Duda GN, et al. 2007. Physiologically based boundary conditions in finite element modelling. *J Biomech* 40:2318–2323.
41. Nicholas T, Zuiker J. 1989. On the use of the Goodman diagram for high cycle fatigue design. *Int J Fract* 80: 219–235.
42. Weinans H, Huiskes R, Grootenboer H. 1992. Effects of material properties of femoral hip components on bone remodeling. *J Orthop Res* 10:845–853.
43. Kuiper J, Huiskes R. 1992. Numerical optimization of hip-prosthetic stem material. In: Middleton J, Pande GN, Williams KR, editors. *Recent advances in computer methods*

- in Biomechanics & Biomedical Engineering. Swansea: Books and Journals International. p 76–84.
44. Heiner AD. 2008. Structural properties of fourth-generation composite femurs and tibias. *J Biomech* 41:3282–3284.
 45. Gruen TA, Mcneice GM, Amstutz HC. 1979. “Modes of failure” of cemented stem-type femoral components: a radiographic analysis of loosening. *Clin Orthop Relat Res* 141:17–27.
 46. Banaszkiwicz PA. 2014. Clinical and radiographic evaluation of total hip replacement. A standard system of terminology for reporting results. In: Banaszkiwicz AP, Kader FD, editors. *Classic papers in orthopaedics*. London: Springer; p 23–26.
 47. Johnston RC, Fitzgerald R, Harris W, et al. 1990. Clinical and radiographic evaluation of total hip replacement. A standard system of terminology for reporting results. *J Bone Joint Surg Am* 72:161–168.
 48. Bombelli R, Mathys R. 1982. Cementless isoelastic RM total hip prosthesis. *J R Soc Med* 75:588.
 49. Trebse R, Milosev I, Kovac S, et al. 2005. Poor results from the isoelastic total hip replacement. *Acta Orthop* 76:169–176.
 50. Glassman AH, Crowninshield RD, Schenck R, et al. 2001. A low stiffness composite biologically fixed prosthesis. *Clin Orthop Relat Res* 393:128.
 51. Hartzband M, Glassman A, Goldberg V, et al. 2010. Survivorship of a low-stiffness extensively porous-coated femoral stem at 10 years. *Clin Orthop Relat Res* 468:433–440.
 52. Akhavan S, Matthiesen MM, Schulte L, et al. 2006. Clinical and histologic results related to a low-modulus composite total hip replacement stem. *J Bone Joint Surg Am* 88:1308–1314.
 53. Khanoki SA, Pasini D. 2011. Multiscale design and multi-objective optimization of orthopaedic cellular hip implants. *Proceedings of the ASME 2011 International Design Engineering Technical Conferences & Computers and Information in Engineering Conference IDETC/CIE 2011*. Washington, DC, USA.
 54. Kuiper J, Huiskes R. 1996. Friction and stem stiffness affect dynamic interface motion in total hip replacement. *J Orthop Res* 14:36–43.
 55. Huiskes R, Weinans H, Grootenboer HJ, et al. 1987. Adaptive bone-remodeling theory applied to prosthetic-design analysis. *J Biomech* 20:1135–1150.
 56. Bougoucha A, Elgaly I, Stukenborg-Colsman C, et al. 2010. Numerical investigations of the strain-adaptive bone remodeling in the prosthetic pelvis. *IFMBE Proceedings* 29. Greece: Springer. p 562–565.
 57. Bodén HS, Sköldenberg OG, Salemyr MO, et al. 2006. Continuous bone loss around a tapered uncemented femoral stem: a long-term evaluation with DEXA. *Acta Orthop* 77:877–885.
 58. Berry DJ, Bozic KJ. 2010. Current practice patterns in primary hip and knee arthroplasty among members of the American Association of Hip and Knee Surgeons. *J Arthroplasty* 25:2–4.

SUPPORTING INFORMATION

Additional supporting information may be found in the online version of this article at the publisher’s web-site.

Supporting Information

Fully porous 3D printed titanium femoral stem to reduce stress-shielding following total hip arthroplasty

Sajad Arabnejad¹, R. Burnett Johnston², Michael Tanzer³, Damiano Pasini^{4}*

¹Arabnejad, SA, Mechanical engineering department, McGill University, Montreal, Quebec, H3A0C3, Canada

²Johnston, RBJ, Mechanical engineering department, McGill University, Montreal, Quebec, H3A0C3, Canada

³ Tanzer, MT, Jo Miller Orthopaedic Research Laboratory, Division of Orthopaedics, Department of Surgery, McGill University, Montreal, Quebec, H3G1A4, Canada

S1: Assigning realistic bone material properties

Computed tomography (CT) data of femoral bone tissues have been used to assign varying materials properties to the physiological finite element (FE) model of the femur. This allows for a representation the heterogeneity intrinsically present in a human femur. To achieve this goal, we use radiographic density of CT images, quantified as Hounsfield Unit (HU), to represent the local material properties of the human femur. CT-scan data are provided through the Visible Human Project (VHP) database of the United States National Library of Medicine (NLM, Bethesda, MD). Since the relationship between HU and bone density is monotonic, we adopt a linear relationship (Figure S1) between bone apparent density and the HU. Bone apparent density is defined as the dry weight of bone divided by the total volume of a given bone sample. Bone effective density, on the other hand, is defined for the condition accounting for the fluid mass. For example, at regions on CT images where there is no bone, the effective density would be about 1024 kg/m^3 , which represents the density of blood. However, both apparent density and HU values of these regions would be zero. Excluding the density of the fluid from bone density ensures fluid density has no contribution to the mechanical properties of the bone. The apparent density ρ for each element of the FE model is then determined from the Hounsfield value (HU) measured from CT data ranging from 0 HU to 1567 HU. The maximum value of HU corresponds to the densest region of the cortical bone with apparent density of 2000 kg/m^3 . From the apparent density distribution, the effective elastic moduli of bone are obtained through the relation¹⁻³:

$$\begin{cases} E = 1904\rho^{1.64} & \rho < 0.95 \\ E = 2065\rho^{3.09} & 0.95 < \rho \end{cases}, \quad \nu = 0.3 \quad (\text{S1})$$

where E is the elastic modulus of the bone, and ν is the Poisson's ratio. Bone is treated here as isotropic material, as this simplification does not lead to a noticeable difference from those results obtained by considering orthotropic properties^{2;3}.

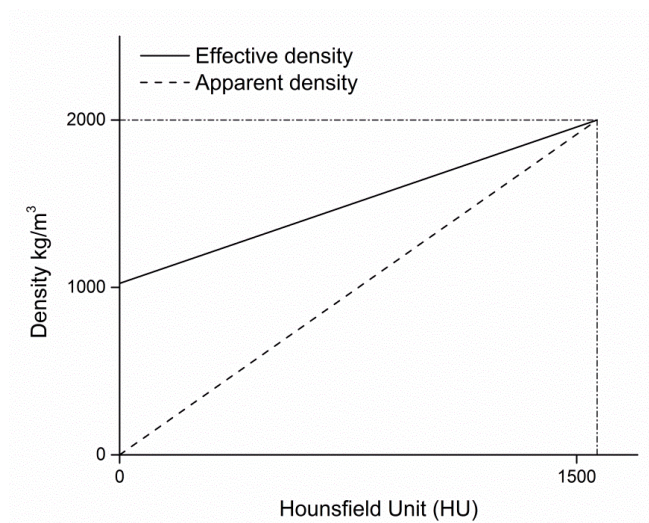


Figure S1: Linear relationship between effective and apparent density, and Hounsfield number.

S2: Homogenized properties of the porous architected material

The mechanical properties of a cellular implant are mainly governed by the properties of its porous architecture. Here the properties of the cellular implant are not obtained through a fully detailed simulation of its porous architecture, as it would be very lengthy and computationally intensive. We therefore used Asymptotic Homogenization (AH) to obtain the effective properties of the porous architecture of the implant. A tetrahedron lattice is considered as the microstructure of the implant. We present here the elastic constants and yield strength of the tetrahedron lattice, which are used for the FE simulations and material density tailoring of the implant. To obtain the effective mechanical properties of the tetrahedron lattice through AH, the following local problem defined on a representative volume element (RVE) is solved^{4;5}:

$$\int_{Y_c} E_{ijpm} \varepsilon_{ij}^1(v) \varepsilon_{pm}^{*kl}(u) dY = \int_{Y_c} E_{ijkl} \varepsilon_{ij}^1(v) \bar{\varepsilon}_{kl} dY \quad (S2)$$

where $\varepsilon_{ij}^1(v)$ is the virtual strain, $\varepsilon_{ij}^{*kl}(u)$ is the microstructural strain corresponding to the component kl of the macroscopic strain tensor ($\bar{\varepsilon}_{kl}$), Y_c is the solid part of the cell, and E_{ijkl} is the local elasticity tensor. We recall that in periodic lattice, the RVE is a limited region of the material whose mechanical properties represent the effective properties of the whole material. The periodicity of field quantities at the microscale is ensured by imposing periodic boundary conditions on the RVE edges; hence the nodal displacements on the opposite edges are set to be equal^{5;6}. Considering the assumption of small deformations and elastic material behavior, the solution of Equation (S2) leads to a linear relation between the macroscopic ($\bar{\varepsilon}_{ij}$) and microscopic (ε_{ij}) strain through the local structural tensor M_{ijkl} :

$$\varepsilon_{ij} = M_{ijkl} \bar{\varepsilon}_{kl}, \quad M_{ijkl} = \frac{1}{2} (\delta_{ik} \delta_{jl} + \delta_{il} \delta_{jk}) - \varepsilon_{ij}^{*kl} \quad (S3a, b)$$

Where δ_{ij} is the Kronecker delta. For a two-dimensional case, three independent unit strains are required to construct the M_{ijkl} matrix. The effective stiffness tensor E_{ijkl}^H is then calculated by the following equation:

$$E_{ijkl}^H = \frac{1}{|Y|} \int_{Y_c} E_{ijpm} M_{pmkl} dY \quad (S4)$$

Where $|Y|$ is the volume of the entire unit cell with voids. The homogenized stiffness matrix relates the macroscopic strains to the macroscopic stresses of the homogenized material. Once the local structure tensor M_{ijkl} is obtained, the microscopic stresses corresponding to the macroscopic strain can be obtained via the following equation:

$$\sigma_{ij} = E_{ijkl} M_{klmn} \bar{\epsilon}_{mn} \quad (S5)$$

Using the homogenized stiffness matrix, the microscopic stress distribution σ_{ij} can be related to the multi-axial macroscopic stress $\bar{\sigma}_{ij}$ by the following relation:

$$\sigma_{ij} = E_{ijkl} M_{klmn} (E_{rsmn}^H)^{-1} \bar{\sigma}_{rs} \quad (S6)$$

The von Mises stress distribution over the microstructure is then used to capture the yield surface of the unit cell expressed as follow:

$$\bar{\sigma}_{ij}^y = \frac{\sigma_{ys}}{\max\{\sigma_{VM}(\bar{\sigma}_{ij})\}} \bar{\sigma}_{ij} \quad (S7)$$

Where $\bar{\sigma}_{ij}^y$ is the yield strength of the unit cell, σ_{ys} is the yield strength of the bulk material, and $\sigma_{VM}(\cdot)$ is the von Mises stress of the microstructure corresponding to the applied macroscopic stress. To obtain yield strength of a cell topology in uniaxial and shear directions, six states of macroscopic stress should be applied:

$$\begin{aligned} \bar{\sigma}_{11} &= [1 \ 0 \ 0 \ 0 \ 0 \ 0], \quad \bar{\sigma}_{12} = [0 \ 0 \ 0 \ 1 \ 0 \ 0] \\ \bar{\sigma}_{22} &= [0 \ 1 \ 0 \ 0 \ 0 \ 0], \quad \bar{\sigma}_{23} = [0 \ 0 \ 0 \ 0 \ 1 \ 0] \\ \bar{\sigma}_{33} &= [0 \ 0 \ 1 \ 0 \ 0 \ 0], \quad \bar{\sigma}_{13} = [0 \ 0 \ 0 \ 0 \ 0 \ 1] \end{aligned} \quad (S8)$$

To obtain the yield strength under bi-axial directions the following macroscopic loading states are applied:

$$\begin{aligned} \bar{\sigma}_{b12} &= [1 \ 1 \ 0 \ 0 \ 0 \ 0] \\ \bar{\sigma}_{b23} &= [0 \ 1 \ 1 \ 0 \ 0 \ 0] \\ \bar{\sigma}_{b13} &= [1 \ 0 \ 1 \ 0 \ 0 \ 0] \end{aligned} \quad (S9)$$

Using Equations S8-9 into Equation S7 allows to obtain the yield strength of the cell topology under uniaxial, shear, and bi-axial loading conditions. The procedure described above is applied to determine the effective mechanical properties of the tetrahedron cell topology used for the implant design⁷. Its effective elastic modulus and yield strength are presented in Figure S2 as a function of relative density. Here, the following notations are used for its yield strength in uniaxial, shear, and bi-axial directions:

$$\begin{aligned}
\bar{\sigma}_{xx}^y &= \bar{\sigma}_{11}^y, \bar{\sigma}_{yy}^y = \bar{\sigma}_{22}^y, \bar{\sigma}_{zz}^y = \bar{\sigma}_{33}^y \\
\bar{\sigma}_{xy}^y &= \bar{\sigma}_{12}^y, \bar{\sigma}_{yz}^y = \bar{\sigma}_{23}^y, \bar{\sigma}_{xz}^y = \bar{\sigma}_{13}^y \\
\bar{\sigma}_{bxy}^y &= \bar{\sigma}_{b12}^y, \bar{\sigma}_{byz}^y = \bar{\sigma}_{b23}^y, \bar{\sigma}_{bxz}^y = \bar{\sigma}_{b13}^y
\end{aligned}
\tag{S10}$$

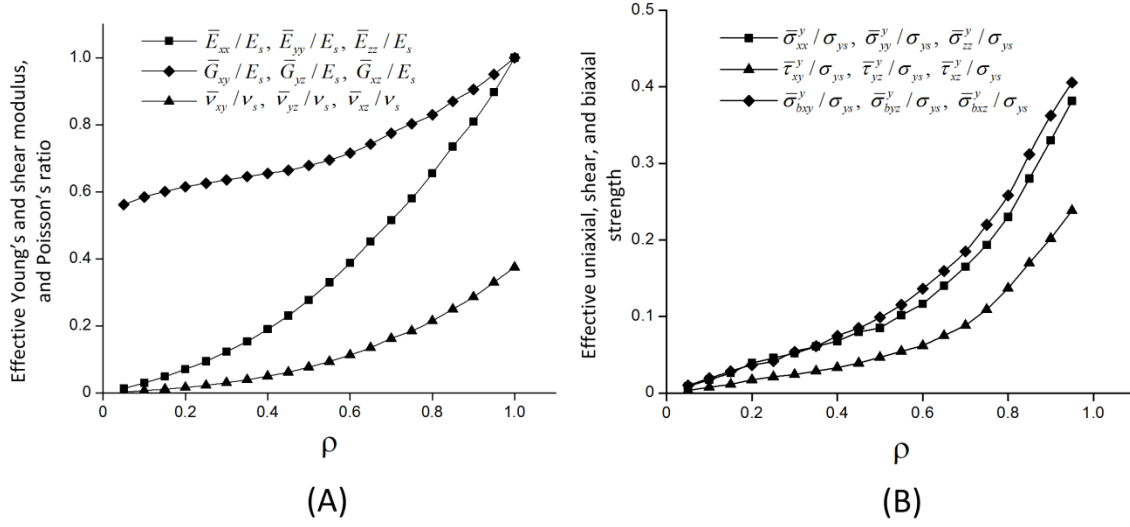


Figure S2. (A) Effective elastic and (B) effective strength properties of a tetrahedron cell as a function of relative density. The effective elastic properties and yield strengths are normalized with the elastic properties and the yield strengths of the bulk material.

S3: Relative density distribution throughout the implant

One of the main goal of this work is to search for an optimum relative density distribution throughout the implant that can minimize bone resorption secondary to stress shielding. We discretize the 3D implant domain with 75 sampling points on the medial-lateral plane of the implant, as shown in Figure S3. The relative densities of these 75 points constitute the vector of the design variables. To obtain the relative density distribution throughout the implant, we considered four sampling points as a 4-node bilinear quadrilateral element. The relative density of each element of the implant FE model is then obtained from the linear interpolation between the relative densities of the nodes of the 4-node bilinear element as follows:

$$\rho_{elem} = \sum_i^{i+3} w_i \rho_i \quad (S11)$$

ρ_i is the relative density at sampling points, and ρ_{elem} is the relative density of each element of the implant finite element model. w_i is the weighting factor obtained from the shape function definition of a 4-node bilinear quadrilateral element. The location of the element center with respect to the local coordinates of the 4-node bilinear quadrilateral element is used to evaluate the weighting factors w_i .

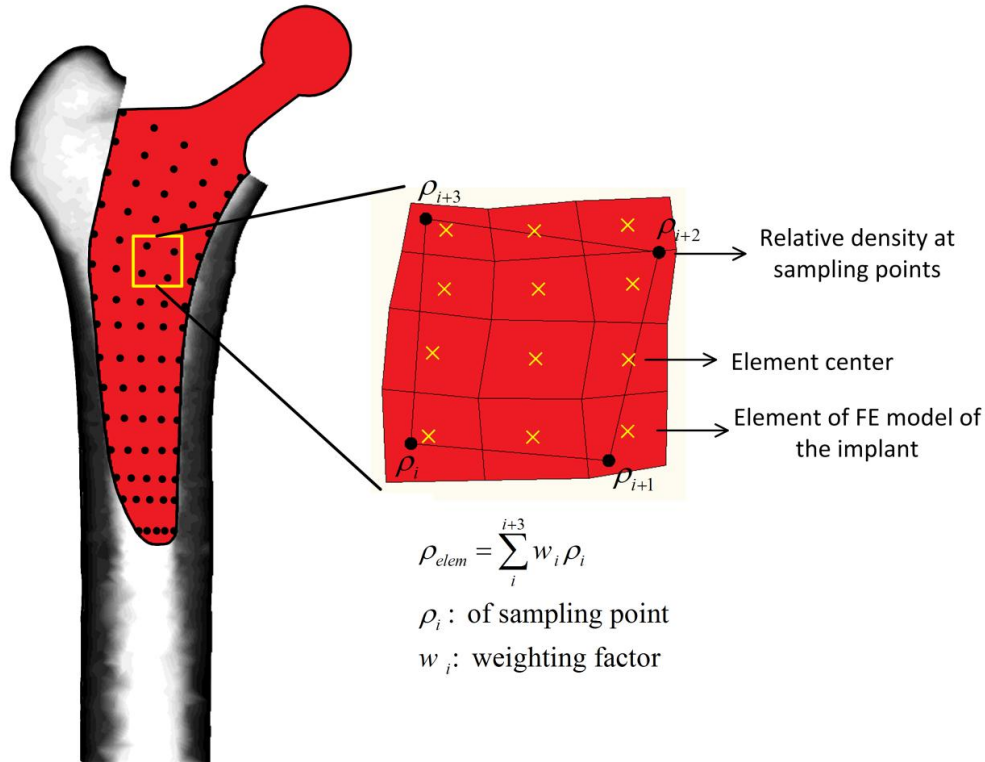


Figure S3. Calculation of the relative density distribution throughout the implant from linear interpolation between the relative densities at the sampling points

S4: a) Tsai-Wu Failure criterion

To obtain the yield strength of a Tetrahedron lattice under multiaxial loading conditions, the local problem defined in Equation S2 should be solved. However, this process can be significantly time consuming as Equation S2 should be solved for any loading direction. As an alternative, we use the Tsai-Wu failure criterion for the failure analysis of the tetrahedron lattice under multiaxial conditions. The Tsai–Wu failure criterion is a material failure metric which is widely used for anisotropic materials, especially for composites. The Tetrahedron-based cell used for the hip implant architecture has three planes of symmetry; therefore, the general form of the Tsai-Wu failure criterion reduces to ⁸:

$$F_i \bar{\sigma}_i + F_{ij} \bar{\sigma}_i \bar{\sigma}_j \leq 1 / SF \quad (S12)$$

Where $i, j = 1 \dots 6$ are repeated indices to indicate summation, and F_i, F_{ij} are experimentally determined material strength parameters. The stresses $\bar{\sigma}_i$ are expressed in Voigt notation.

For orthotropic materials with three planes of symmetry, if we assume that $F_{ij} = F_{ji}$ and no coupling exists between the normal and shear stress terms, the general form of the Tsai–Wu failure criterion reduces to:

$$\begin{aligned} F_1 \bar{\sigma}_1 + F_2 \bar{\sigma}_2 + F_3 \bar{\sigma}_3 + F_4 \bar{\sigma}_4 + F_5 \bar{\sigma}_5 + F_6 \bar{\sigma}_6 \\ F_{11} \bar{\sigma}_1^2 + F_{22} \bar{\sigma}_2^2 + F_{33} \bar{\sigma}_3^2 + F_{44} \bar{\sigma}_4^2 + F_{55} \bar{\sigma}_5^2 + F_{66} \bar{\sigma}_6^2 \\ + 2F_{12} \bar{\sigma}_1 \bar{\sigma}_2 + 2F_{13} \bar{\sigma}_1 \bar{\sigma}_3 + 2F_{23} \bar{\sigma}_2 \bar{\sigma}_3 \leq 1 / SF \end{aligned} \quad (S13)$$

We assume the yield strengths of the unit cell in tension and compression are equal, and the yield strength in the x, y, z directions can be noted as $\bar{\sigma}_{xx}^y, \bar{\sigma}_{yy}^y, \bar{\sigma}_{zz}^y$. We also assume the shear strengths in the three planes of symmetry have identical magnitude even if the signs are different, and are noted as $\bar{\sigma}_{xy}^y, \bar{\sigma}_{yz}^y, \bar{\sigma}_{xz}^y$. The coefficients of the Tsai–Wu failure criterion for an orthotropic material are:

$$F_1 = F_2 = F_3 = F_4 = F_5 = F_6 = 0 \quad (S14)$$

$$F_{11} = \frac{1}{(\bar{\sigma}_{xx}^y)^2}, F_{22} = \frac{1}{(\bar{\sigma}_{yy}^y)^2}, F_{33} = \frac{1}{(\bar{\sigma}_{zz}^y)^2}$$

$$F_{44} = \frac{1}{(\bar{\sigma}_{xy}^y)^2}, F_{55} = \frac{1}{(\bar{\sigma}_{yz}^y)^2}, F_{66} = \frac{1}{(\bar{\sigma}_{xz}^y)^2}$$

The coefficients F_{12} , F_{23} , F_{13} can be determined using equibiaxial tests. If the failure strengths in equibiaxial tension are $\bar{\sigma}_1 = \bar{\sigma}_2 = \bar{\sigma}_{bxy}^y, \bar{\sigma}_1 = \bar{\sigma}_3 = \bar{\sigma}_{bxz}^y, \bar{\sigma}_2 = \bar{\sigma}_3 = \bar{\sigma}_{byz}^y$ then:"

$$F_{12} = \frac{1}{2(\bar{\sigma}_{bxy}^y)^2} \left[1 - (\bar{\sigma}_{bxy}^y)^2 (F_{11} + F_{22}) \right]$$

$$F_{23} = \frac{1}{2(\bar{\sigma}_{byz}^y)^2} \left[1 - (\bar{\sigma}_{byz}^y)^2 (F_{22} + F_{33}) \right] \quad (S15)$$

$$F_{13} = \frac{1}{2(\bar{\sigma}_{bxz}^y)^2} \left[1 - (\bar{\sigma}_{bxz}^y)^2 (F_{11} + F_{33}) \right]$$

b) Design of porous microstructure of the implant against fatigue failure

As a result of patient activities, a hip implant undergoes repeated cyclic loading. To avoid progressive and localized damage caused by daily cyclic loading, the prosthesis is designed for fatigue under high cycle regime. To design against fatigue failure, we assume the lattice microstructure to be free of defects, such as scratches, notches and nicks. As a result, the constant life diagram can be constructed to verify and design the lattice against fatigue failure⁹. For the material properties of the lattice, we consider Ti6Al4V with mechanical properties: 900 MPa for the yield strength of the solid material, 200 MPa for the fatigue strength at 10^7 cycles, 120 GPa for the Young's modulus, and 0.3 for the Poisson's ratio. These properties are experimental values obtained from high cycle fatigue testing of Ti6Al4V samples manufactured by SLM¹⁰. The yield strength and endurance limit of the lattice are used to construct the Soderberg diagram for the fatigue analysis under multiaxial loading:

$$\frac{\|\{\bar{\sigma}^m\}\|}{\|\{\bar{\sigma}^y\}\|} + \frac{\|\{\bar{\sigma}^a\}\|}{\|\{\bar{\sigma}^e\}\|} = \frac{1}{SF} \quad (S16)$$

where $\|\square\|$ denotes the second norm operator to compute the vector length, $\{\bar{\sigma}^y\}$ is the yield strength of the lattice for the given loading condition, and it is obtained from the Tsai-Wu failure criterion. $\{\bar{\sigma}^e\}$ is the endurance limit of the lattice computed from the yield strength through the following equation:

$$\{\bar{\sigma}^e\} = \{\bar{\sigma}^y\} \frac{\sigma_{es}}{\sigma_{ys}} \quad (\text{S17})$$

$\{\bar{\sigma}^m\}$ and $\{\bar{\sigma}^a\}$ are, respectively, the mean and alternating macroscopic stresses and are calculated with the following relations:

$$\{\bar{\sigma}^m\} = \frac{\{\bar{\sigma}^{\max}\} + \{\bar{\sigma}^{\min}\}}{2}, \quad \{\bar{\sigma}^a\} = \frac{\{\bar{\sigma}^{\max}\} - \{\bar{\sigma}^{\min}\}}{2} \quad (\text{S18 a, b})$$

where $\{\bar{\sigma}^{\max}\}$ and $\{\bar{\sigma}^{\min}\}$ are the multiaxial macroscopic stresses that cause, respectively, the highest and the lowest values of the von Mises stress in the microstructure.

S5: Measures of Bone loss and interface failure index

The amount of bone loss around the stem is determined by assessing the amount of bone that is under loaded post implantation relative to the intact femur. Bone can be considered locally under loaded when its local strain energy (U) per unit of bone mass (ρ) ($S = \frac{U}{\rho}$), is beneath the local reference value S_{ref} , which is the value of S when no prosthesis is present. However, it has been observed that not all the under loading leads to resorption, and a certain fraction of under loading (the threshold level or dead zone s) is tolerated. Bone resorption starts when the local value of S is beneath the value of $(1-s)S_{ref}$ ^{11; 12}. Using this definition, the resorbed bone mass fraction m_r can be obtained from:

$$m_r(\mathbf{b}) = \frac{1}{M} \int_V g(S(\mathbf{b})) \rho dV \quad (\text{S19})$$

where M and V are the original bone mass and volume respectively, and $g(S(\mathbf{b}))$ is a resorptive function equal to unity if the local value of S is beneath the local value of $(1-s)S_{ref}$ and equal to 0 if $(1-s)S_{ref} < S$. In this study, the value of dead zone s is set to be 0.75¹².

The interface failure $f(\sigma_k^b)$ is expressed by the following relation:

$$f(\sigma_k^b) = \frac{\tau}{S_s} < 1 \quad (\text{S20})$$

where τ is the local shear stress at the bone-implant interface, and S_s is the bone shear strength.

In Equation S19, the interface failure $f(\sigma_k^b)$ is constrained to be lower than one to ensure the bone-implant interface failure will not occur. The shear strengths of bone can be expressed as a function of bone apparent density according to the power law relation obtained by Pal et al.¹³:

$$S_s = 21.6\rho^{1.65} \quad (\text{S21})$$

The bone apparent relative density is measured from HU of CT-scan images, as described in the Supporting Information S1.

S6: Femoral Potting

All femoral condyles were resected at a distance of 22 cm measured from the tip of the greater trochanter. Using a customized stand, the femurs were angled at 12 degrees flexion, and 12 degrees adduction, as measured by a plumb weight and goniometer. Using Suprastone (Kerr Group, Charlotte, NC) dental cement, a mold of the distal femur was created to serve as a supplement to the angle measurement. This choice ensured added consistency in the femoral orientation and positioning in addition to the plumb weight and goniometer angle measurement. The distal segment of the femurs was cleaned with 70% isopropyl alcohol and lowered into the center of a 10.2 cm diameter polyethylene container. The femur was lowered into the container until the distal aspect of the femur was 13 mm from the base of the container, and positioned such that the center of the femoral shaft corresponded with the center of the container. A total of 350 ml of epoxy (3M, Saint Paul, MN) was then added to the container in two phases. For the first phase an initial volume of 250 ml was added to stabilize the femur. After one hour started the second phase, which consisted of an additional 100 ml. For both phases the mixtures consisted of a ratio of 80:1 resin to hardener. The process was conducted in two distinct phases to avoid cracking of the epoxy layer, which can occur if the layer thickness is greater than 12.5 mm due to the exothermic effect of polymerization. The construct was allowed to harden for at least 24 hours. The process was repeated for all six femurs.

S7: Femoral Painting

DIC relies on the contrast between speckles and the surrounding surface; it correlates the motion and deformation of the surface and calculate the strain ¹⁴. The color of the artificial femurs is a dark brown that does not provide sufficient contrast for either black or white speckle patterns. As such, a base coating of white aerosol paint was applied in 3 layers, with particular care to provide a consistent finish on the medial calcar of the femur. A black speckle pattern was then applied to the femoral surface with speckles ranging from 500-1000 microns by means of sputtering aerosol paint. For DIC the best correlations can be obtained when the ratio of speckles to background is roughly 50%. After speckling, any areas without sufficient speckle density had individual speckles added by hand, especially in areas of high curvature to avoid aerosol speckle streaking.

S8: Implantation processes for composite femur

After completing the DIC loading, the intact femurs were removed from the loading jig. An anteroposterior radiograph of the intact femur was taken and used to template the hip in order to determine the implant size, implant neck offset and neck length needed to ensure complete canal filling by the implant and to restore the normal biomechanics of the proximal femur. All the surgeries were performed by an experienced orthopaedic surgeon (Author MT) using standard operative equipment supplied by Depuy (DePuy-Synthes, Warsaw, IN). From the pre-operative template measurements, the femurs were marked with the neck osteotomy guide at a height of 8mm from the top of the lesser trochanter, and the femoral head and neck were resected. The femurs were then inserted into another jig to stabilize their position for implantation (Figure S5). The canal was broached with a long curette and a trochanteric rasp was used to ensure anatomic lateralization of the femoral component. The canal was then rasped progressively until a size 6 rasp (based on the templating) was well seated. After preparation, the femur received either a fully porous, or a solid control femoral stem implant.

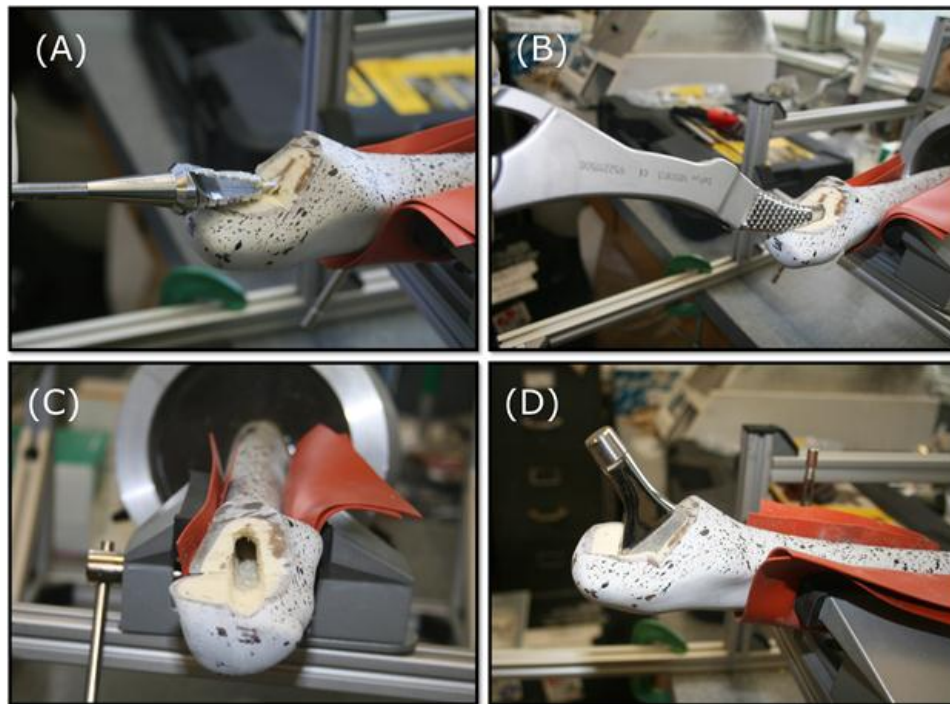


Figure S5. Insertion of femoral components. A) Removing excess bone at the greater trochanter to avoid Varus stem position. B) The femur is broached with successive rasps up to size 6. C) Prepared canal shows proper anteversion. D) Stem after implantation in the artificial femur.

Due to a substantial physical effort required to implant the femurs, the implantations were conducted in pairs, with one femur receiving a fully porous stem and the other a fully solid control stem. An Anterior-Posterior (AP) and Medial-Lateral (ML) projection radiograph were taken to ensure consistent implant position, and to correct the length of the neck offset (Figure

S6). The implanted femurs were mounted on the same loading jig, and loading and image acquisition procedure were repeated.

S9: Assessment of Implant Size

In this study, the geometry of the Trilock Bone Preserving Stem (Depuy-Synthes, Warsaw, IN) is used for the design of a hip implant with porous tailored architecture to reduce stress shielding. The macro geometry of the Trilock BPS stem is designed to have a minimally invasive shape and to achieve metaphyseal contact with the cortical bone to transmit load to the proximal femur¹⁵. To provide a proper fixation and restore the kinematic motion of the natural joint, the choice of the correct implant size is imperative. Another critical parameter is the recovering of the appropriate neck offset. In an operative situation, restoring the hip biomechanics as accurately as possible is essential, besides achieving proper leg length to avoid discrepancies that can negatively impact gait and result in dislocation. This is crucially important for any biomechanical study, such as this work, since the neck offset governs the moment arm of the force applied on the femoral head. If the femoral neck offset is reduced after implantation, it leads to an overall lower strain on the proximal femur, relative to the intact femur, due to the decreased moment. Likewise, if the offset is too large, it will underestimate the effect of stress shielding. Studies that do not account for variations of femoral neck offset can be misleading, because the change in strain is a result of the offset, as opposed to the implant performance¹⁶.

To account for the factors described above, all femurs were radiographed in the anterior posterior direction so as to determine neck offset and stem size. The neck offset was measured in a three step process that is widely used for radiological analysis¹⁷. The first step consists of measuring the width of the proximal femoral canal at two locations, and marking the center point of the canal at two levels. The two points are then connected to serve as the centerline of the femoral axis. Next, the center of the femoral head is marked by means of fitting a template circle to the intact femoral head. Finally, a line is drawn orthogonally from the femoral axis to the marked center of the femoral head. The distance along this line from the center of the femoral head to the centerline of the femoral shaft is the effective neck offset. The implant size was selected based on operative templates provided by Depuy-Synthes (Warsaw, IN) and the judgment of an experienced orthopedic surgeon (MT) and chosen to be a size 6 high offset. To confirm the implant size, the femur was broached with progressively larger rasps until the size six rasp was seated. Another radiograph was taken, with the rasp left in the femur. Both medial and lateral contact between the rasp and the cortical bone was monitored, and the assessment indicated that the size was appropriate. Once the implant size was determined, the neck offset and femoral head component were appropriately selected from the sizing information provided by Depuy. The implant size was determined as a size 6 H (high or extended neck offset) with a +5 32 mm diameter femoral head.

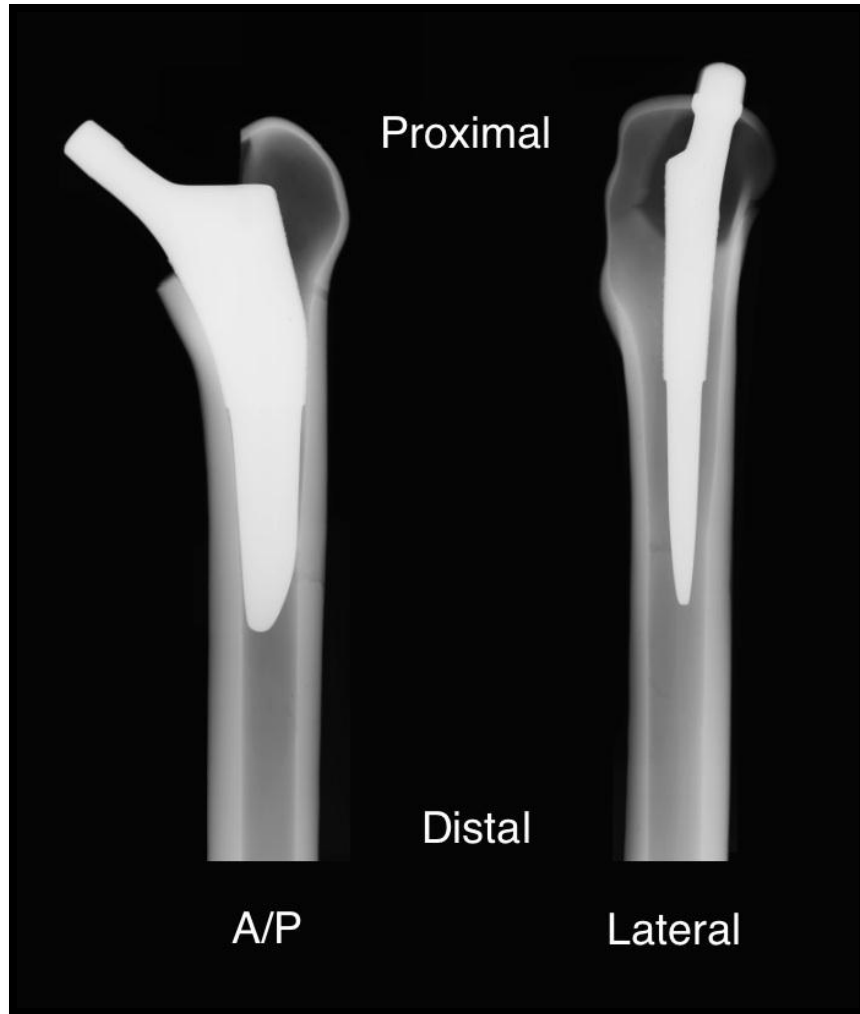


Figure S6. Anterior Posterior and Medial Lateral Radiograph showing the proper implant fit

S10: Digital Image correlation and Image registration to an Atlas using MATLAB

VIC3D (Correlated Solutions, Irmo, SC) was used to run the digital image correlation on the obtained data sets. To process the images, an oversized rectangular Area of Interest (AOI) was drawn around the complete femur to extract all possible data, and a subset size of 20 pixels, with a 5 pixel step, was used with a strain smoothing filter of 15 pixels. The correlation was run for all images within the sequence. Calibration was performed using a 9X12 circular pattern with 9 mm spacing using a grid generated by VIC 3D. This grid size was chosen to fill up the majority of the field of view in order to provide the best calibration for the system. Despite the rigid camera fixation to the load frame, the calibrations were repeated during the analysis of the implanted femurs so as to avoid the risk of camera movement after femur removal from the load set up. Because the investigation pertained to the loaded state of the femur, the images during the 2300N loading plateau were selected and exported to Matlab for further processing. The data obtained during transient stage of loading and unloading were not used in the analysis.

The exported data files provide the position and strain for each subset of point of the DIC analysis. The average principle compressive strain and standard deviation was calculated for each subset over the images obtained during the fully loaded phase of the gait cycle. If a subset within any image deviated by more than three standard deviations from the mean, it was removed from the data set, and the average recalculated. For further processing, the data were reformatted into a rich point cloud (RPC). The RPC consisted of a cloud of points with xyz coordinates of the subsets, along with their corresponding average values of principle compressive strain.

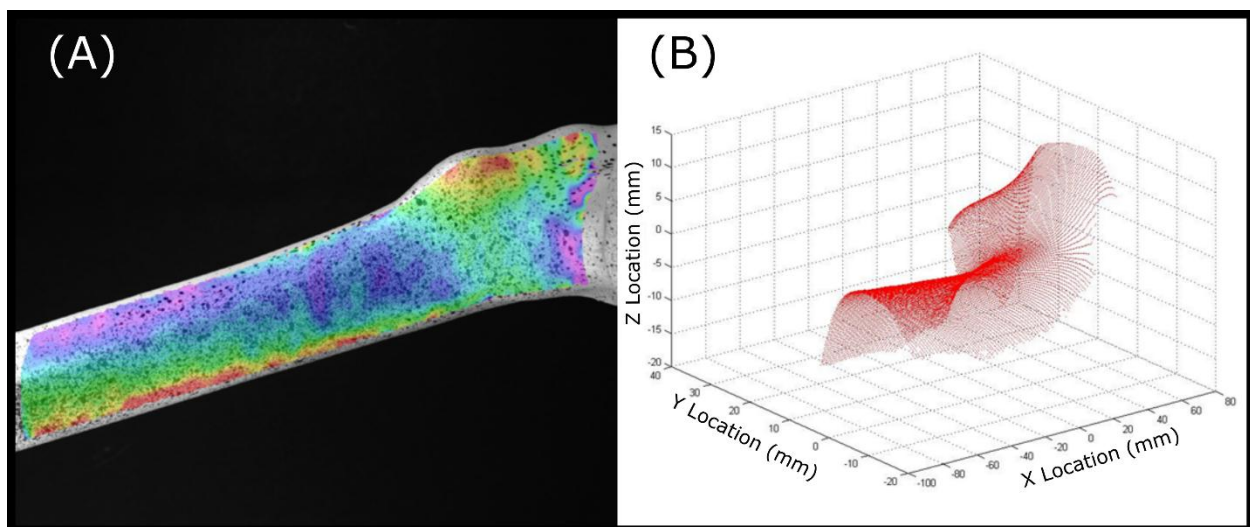


Figure S71: Exporting native DIC data to a rich point cloud format in Matlab. A) Compressive strain on the original DIC image. B) Data exported as a rich point cloud for further analysis.

To ensure consistent positioning of the data, the RPC was registered to an atlas reference of the composite femur. This was achieved through means of a rigid body registration using an iterative

closest point method with KD Tree logic and plane minimization to improve accuracy¹⁸. The results of the registration were manually inspected to ensure that registration was appropriate. The registration of the data set to a reference femur insured that the local strain measurement was consistently anatomically located. A 20 pixel subset with a five pixels step size was used with a pixel size of approximately 100 microns. This corresponds to a grid of data points along the surface of the medial calcar spaced approximately 500 microns apart. The registration procedure of each data set to the reference femur atlas provided a consistent reference for comparison between each treatment group.

The absolute strain was not verified relative to a strain gauge in this experiment. However, previous work by Gilchrist et al has shown reasonable agreement between strain gauges and DIC and indicates that DIC is appropriate for complex geometries such as human bone¹⁹. Furthermore, the experimental model presented in this work is not estimating the true strain of the femur; rather, it evaluates the relative strain between an intact and implanted femur. Because the field quantity of interest in this work is the change of strain, and not the absolute strain, any bias of the DIC experimentation could be removed. This was also ensured by the use of a rigid jig fixing the cameras to the load frame, as well as the 3D DIC acquired with synchronized stereoscopic image acquisition. As a result, errors that can be introduced by deviations along the optical axis of the camera were avoided²⁰.

S11: Surface bone loss measurement from DIC experiment

In the DIC experiment, only the changes of strain on the medial calcar of the composite femur were considered. Due to the loading condition at the hip joint, the main deformation mechanism of the bone is bending with medial calcar under compression strain. Therefore, the principle compressive strain can be calculated as the strain before and after implantation to assess the amount of bone loss. To be consistent with strain energy measurements used in bone loss measurement during the design process, we considered as a metric for bone resorption, the ratio of post implantation surface strain to the pre implantation surface strain squared. The strain energy of bone can be related to strain through the relation:

$$S = \frac{1}{2} \int_V \{\varepsilon\}^T [E] \{\varepsilon\} dV \quad (S22)$$

where $\{\varepsilon\}$ is the strain tensor, and $[E]$ is the stiffness tensor. Using the principle compressive strain, we can roughly estimate the strain energy of each element as follows:

$$S_{elm} = \frac{1}{2} \varepsilon_{pc}^2 E V_{elm} \quad (S23)$$

where S_{elm} is the strain energy of an element, ε_{pc} is the principle compressive strain, E is the Young's modulus of the element material, and V_{elm} is the element volume. If we consider S_{ref} as the local strain energy before implantation, the ratio of the strain energy after and before implantation is:

$$\frac{S_{elem}}{S_{ref}} = \left(\frac{\varepsilon_{pc}}{\varepsilon_{pc(ref)}} \right)^2 \quad (S24)$$

Eq. S23 shows that the strain energy before and after implantation can be related to the ratio of the post implantation surface strain and the pre implantation surface strain squared. Therefore, in this work Equation 23 was adopted as metric for bone loss measurement on the surface of the composite femur. For quantitative evaluation, the medial calcar was divided into the standardized Gruen zones 7, 6, and 5, with the edges excluded due to the increased noise from subsets that are more than 15 degrees out of the plane of the camera. If the reduction of strain after implantation was greater than 50% relative to the intact femur, the subset was deemed to be prone to bone resorption. This reduction of strain would result in 75% reduction of strain energy of the element according to Equation S23. This condition is equivalent to consider a dead zone of $s=0.75$ for the surface bone loss measurement similar to the volumetric bone loss measurement used in Equation S18. The percentage of subsets within each zone susceptible to resorption was calculated for each Gruen zone, and for each of the individual femurs. The average percentage of bone susceptible to bone resorption was calculated for each Gruen zone; similarly, the average of the Gruen zones for each treatment was calculated. To compare the performance of the implant

type, each Gruen zone was compared using an unpaired student t test with unequal variance, with statistical significance set at $P < 0.05$.

References

1. Austman RL, Milner JS, Holdsworth DW, et al. 2008. The effect of the density–modulus relationship selected to apply material properties in a finite element model of long bone. *Journal of biomechanics* 41:3171-3176.
2. Baca V, Horak Z, Mikulenk P, et al. 2008. Comparison of an inhomogeneous orthotropic and isotropic material models used for FE analyses. *Medical engineering & physics* 30:924-930.
3. Peng L, Bai J, Zeng X, et al. 2006. Comparison of isotropic and orthotropic material property assignments on femoral finite element models under two loading conditions. *Medical engineering & physics* 28:227-233.
4. Guedes J, Kikuchi N. 1990. Preprocessing and postprocessing for materials based on the homogenization method with adaptive finite element methods. *Computer methods in applied mechanics and engineering* 83:143-198.
5. Hollister S, Kikuchi N. 1992. A comparison of homogenization and standard mechanics analyses for periodic porous composites. *Computational Mechanics* 10:73-95.
6. Hassani B. 1996. A direct method to derive the boundary conditions of the homogenization equation for symmetric cells. *Communications in numerical methods in engineering* 12:185-196.
7. Kalamkarov AL, Andrianov IV, Danishevs'kyy VV. 2009. Asymptotic homogenization of composite materials and structures. *Applied Mechanics Reviews* 62:030802.
8. Tsai SW, Wu EM. 1971. A general theory of strength for anisotropic materials. *Journal of composite materials* 5:58-80.
9. Nicholas T, Zuiker J. 1989. On the use of the Goodman diagram for high cycle fatigue design. *International Journal of Fracture* 80:219-235.
10. Wycisk E, Emmelmann C, Siddique S, et al. 2013. High cycle fatigue (HCF) performance of Ti-6Al-4V alloy processed by selective laser melting. *Advanced Materials Research: Trans Tech Publ*; pp. 134-139.
11. Weinans H, Huiskes R, Grootenboer H. 1992. Effects of material properties of femoral hip components on bone remodeling. *Journal of Orthopaedic Research* 10:845-853.
12. Kuiper J, Huiskes R. 1992. Numerical optimization of hip-prosthetic stem material. *Recent Advances in Computer Methods in Biomechanics & Biomedical Engineering* J Middleton, GN Pande, and KR Williams:76–84.
13. Pal B, Gupta S, New A. 2009. A numerical study of failure mechanisms in the cemented resurfaced femur: effects of interface characteristics and bone remodelling. *Proceedings of the Institution of Mechanical Engineers, Part H: Journal of Engineering in Medicine* 223:471-484.
14. Sutton MA, Orteu JJ, Schreier H. 2009. *Image correlation for shape, motion and deformation measurements: basic concepts, theory and applications*: Springer Science & Business Media;
15. Mallory TH, Head WC, Lombardi Jr AV. 1997. Tapered design for the cementless total hip arthroplasty femoral component. *Clinical orthopaedics and related research* 344:172.
16. Cristofolini L, Viceconti M. 1999. In vitro stress shielding measurements can be affected by large errors. *The Journal of arthroplasty* 14:215-219.
17. Lecerf G, Fessy MH, Philippot R, et al. 2009. Femoral offset: Anatomical concept, definition, assessment, implications for preoperative templating and hip arthroplasty. *Orthopaedics & Traumatology: Surgery & Research* 95:210-219.
18. Kjer HM, Wilm J. 2010. Evaluation of surface registration algorithms for PET motion correction. Technical University of Denmark.

19. Gilchrist S, Guy P, Crompton PA. 2013. Development of an Inertia-Driven Model of Sideways Fall for Detailed Study of Femur Fracture Mechanics. *Journal of Biomechanical Engineering* 135:121001-121001.
20. Grassi L, Isaksson H. 2015. Extracting accurate strain measurements in bone mechanics: A critical review of current methods. *Journal of the Mechanical Behavior of Biomedical Materials* 50:43-54.